Thermal Characterization of Magnetic Components in Still Air

Bruno Bertoldi, *Graduate Student Member, IEEE*, Lucas Andrade Militão, *Graduate Student Member, IEEE*,
Gean Jacques Maia de Sousa, *Member, IEEE*, Jader Riso Barbosa Jr.,
and Marcelo Lobo Heldwein, *Senior Member, IEEE*

***Abstract*—Accurate measurement of losses in magnetic components and the resulting temperature behavior is essential for device characterization and thermal model validation. However, some factors such as the significant phase displacement angle between voltage and current, and the practical challenges of measuring high-frequency electrical quantities need to be considered when choosing excitation equipment, probes, and assembling test setups. This work proposes an experimental and noninvasive procedure for acquiring temperatures of magnetic components in stagnant air with prescribed constant input power. The electrical modeling of the system, the choice of suitable equipment and probes for measuring losses, the structure of the system, pretest procedures, and other system components are discussed in detail. The validation of the procedure and the experimental setup was performed through testing of E-core and toroidal inductors, altogether with computational fluid dynamics simulations for an extended range of power losses. Finally, the results presented an excellent agreement, proving that the proposed methodology is a reliable tool for assessing the thermal behavior of magnetic components.**

***Index Terms*—Computational fluid dynamics (CFD) simulation, losses measurement, magnetic components, temperature rise measurement, thermal characterization.**

I. Introduction

THE thermal modeling of components used in power electronics is essential in product development to ensure safety and reliability. This task is considerably less complex for noncustom components, such as semiconductors and capacitors, for which manufacturers have proposed and validated extensive thermal test procedures.

On the other hand, the thermal analysis of custom components, particularly the magnetic ones, can be more challenging given the different design possibilities, such as different types of materials and core or winding geometries. In addition, the characteristics of the core materials have an electrical and thermal nonlinear behavior, which are specific to each material, making the modeling more difficult.

Despite the growing literature and increasing number of thermal models available, assembling a reliable system for validation of thermal models is not trivial. As detailed models contain separate inputs for different kinds of losses, proper validation requires the measurement of the component's thermal response while accurately imposing known losses on the core and windings. This requires a carefully designed experiment.

One of the main experimental challenges is appropriately measuring the component losses. Among the different methods, the thermal approach is one of the best known, where various calorimetric techniques can be applied [1], [2], [3]. However, the processes are too slow to be used in a control loop regulating dissipated power. Transient response calorimetric measurements have been proposed to shorten the measurement times [4], [5], but would be inappropriate to measure the temperature and power losses of the magnetics in the operating conditions considered in the methodology proposed in this study, given how the operating conditions in these setups diverge from the one considered in this study: A magnetic positioned in a circuit board, dissipating heat in still air. The classic wattmeter method is an alternative that consists of obtaining core losses by measuring the magnetic flux variation through an auxiliary winding [6], [7], [8], [9], [10], [11]. Although the losses change with the component temperature (making thermal stabilization a vital aspect of a successful measurement), this method allows rapid assessment of the losses. Unlike the calorimetric method, the generally much faster wattmeter approach does not require the entire system to be in thermal equilibrium. Yet, while good precision can be obtained, its practical implementation requires appropriate instrumentation to avoid errors. The major challenge of the wattmeter approach is the phase displacement between the voltage and current waveforms, which is close to 90°. The measured power is highly sensitive to phase variations in this angle range, where inaccuracies arising from factors such as probes with different time delays and low oscilloscope sampling frequency and accuracy can lead to relevant uncertainties [12], [13].

Manuscript received 10 October 2022; revised 25 January 2023; accepted 24 February 2023. Date of publication 6 March 2023; date of current version 20 April 2023. This work was supported in part by the Coordenação de Aperfeiçoamento de Pessoal de Nível Superior - Brasil (CAPES) - Finance Code 001 and in part by the Conselho Nacional de Desenvolvimento Científico e Tecnologico - Brasil (CNPq) under Sanction 22(0836)/20/EMR-II. Recommended for publication by Associate Editor Minjie Chen. *(Corresponding author: Bruno Bertoldi.)*

Bruno Bertoldi is with the Power Electronics Institute, Federal University of Santa Catarina, Florianopolis 88040-900, Brazil (e-mail: bertoldi.br@gmail.com).

Lucas Andrade Militão and Jader Riso Barbosa Jr. are with the Department of Mechanical Engineering, Federal University of Santa Catarina, Florianopolis 88040-900, Brazil (e-mail: lucas.militao@polo.ufsc.br; jrb@polo.ufsc.br).

Gean Jacques Maia de Sousa and Marcelo Lobo Heldwein are with the Chair of High-Power Converter Systems, Technical University of Munich, 80333 Munich, Germany (e-mail: gean.sousa@tum.de; marcelo.heldwein@tum.de).

Color versions of one or more figures in this article are available at https://doi.org/10.1109/TPEL.2023.3253076.

Digital Object Identifier 10.1109/TPEL.2023.3253076

To overcome the phase lag issue, a compensation technique based on the addition of capacitors has been proposed [12], [13], [14], [15]. Although there are several practical ways to realize this procedure, some care and consideration are required. Since the cancelation is effective only in a short frequency range, winding losses are not easily compensated, giving rise to distortions if the capacitor values are not well designed [12]. Furthermore, structures that only use series capacitors present a very small equivalent impedance, which limits the maximum power that can be applied to the component due to impedance mismatch.

Another problem is the high frequency needed to impose significant losses (up to tens of watts) in the core. Effects caused by the parasitic capacitances between windings themselves and the core can influence the measurements depending on the frequency range. Strategies such as shielding and increasing the distance between windings can be adopted. These suggestions, however, create new challenges from a thermal point of view, since shielding layers influence the heat dissipation to the environment. In addition, the need for a greater distance between the primary and secondary windings prevents a homogeneous distribution of the excitation winding around the core, causing a temperature imbalance in the component. From experiments, depending on the test conditions and core sizes, this effect increased the maximum absolute temperature in the component body by about 10 °C when compared to a homogeneous winding structure.

In addition to the aforementioned challenges of measuring losses, the temperature measurement approach must also be chosen carefully, including the type of environment surrounding the device under test (DUT). Some authors relied on a method proposed in JESD 51-2A [16] to evaluate temperatures and validate compact thermal models of small package electronic components under natural convection [17], [18], [19]. The method recommends measuring temperatures directly using thermocouples and positioning the DUT at the center of an enclosure lined with high emissivity insulating materials. However, magnetic components can be of different sizes, adding difficulties when measuring temperature directly. Depending on the core dimensions and windings arrangement, the thermal distribution is hardly homogeneous, complicating thermal sensor installation, especially when the hottest spots need to be determined. In addition, real components have nonplanar, irregular surfaces, complicating the positioning of sensors whose accuracies are very sensitive to contact resistance. One must also consider the measurement system's noise immunity, especially when applying high-frequency excitation signals. During experimentation, thermocouples proved to be very susceptible to interference, and therefore, do not seem to be suitable for this type of application.

Motivated by the need to validate theoretical models for the thermal behavior of magnetic components, we propose an experimental setup capable of imposing a controllable power dissipation in the component, and measuring and evaluating its temperature distributions. Since it is impossible to guarantee that individual losses will be measured separately, one must ensure that they are imposed separately on each element (core or winding). Thus, two tests are performed: 1) ac only and 2) dc only excitation. This allows the evaluation of the effects of winding and core losses separately. For the ac case, an impedance matching network is used to increase the power factor of the inductor, improving power transfer from the amplifier used as an exciter and decreasing the power measurement uncertainty.

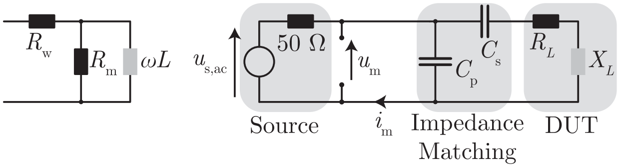

(a) (b)

Fig. 1. (a) Inductor model. (b) Setup for measuring and imposing core losses.

The design of low-cost voltage and current probes suitable for this application is also discussed. An infrared thermal camera and resistance temperature detectors (RTDs) were used for the temperature measurement, which have better noise immunity than thermocouples. The validation of the measurement system is performed by comparing experimental results of a toroidal and E-core inductor with computational fluid dynamics (CFD) simulations using the commercial package ANSYS 15.0.

II. AC EXCITATION

AC excitation is necessary to generate core losses, which also generates winding losses. The latter can be subtracted from the total power measurement to get the core losses. However, winding loss estimation is complex and can add substantial uncertainty to the measurement, especially if it is a significant part of the total losses. Another common approach is the use of an auxiliary winding to measure the voltage across the magnetizing inductance only. However, experimental verification of this method resulted in considerable variations in measured power for the same DUT depending on the arrangement and distance between the excitation winding and the auxiliary winding, which increased with losses and frequency. This effect is mainly caused by the coupling caused by parasitic capacitances. The solution employed in this work consists in minimizing the winding losses to the point that they become negligible when compared to the total loss, which can be measured without auxiliary windings.

For this, an optimization routine is used to define optimal values of inductance L, number of turns N, wire gauge d_b and the ac excitation voltage U_s, and frequency f. The loss calculation is based on the traditional equivalent model consisting of an inductor and two resistors; one representing core losses and the other winding losses, as shown in Fig. 1(a).

To calculate core losses, Steinmetz's equation [20] is used since the excitation is purely sinusoidal. For the calculation of winding losses, an adaptation of classic Dowell's formulation for round conductors is used [21]. An algorithm based on the particle swarm optimization (PSO) concepts [22] was implemented as described in Fig. 2.

Table I exemplary shows how the inductor design influences the ratio between winding and total losses. Each line represents a different design and the necessary voltage and frequency excitation that produces a power dissipation of 10 W in a C0551952 A

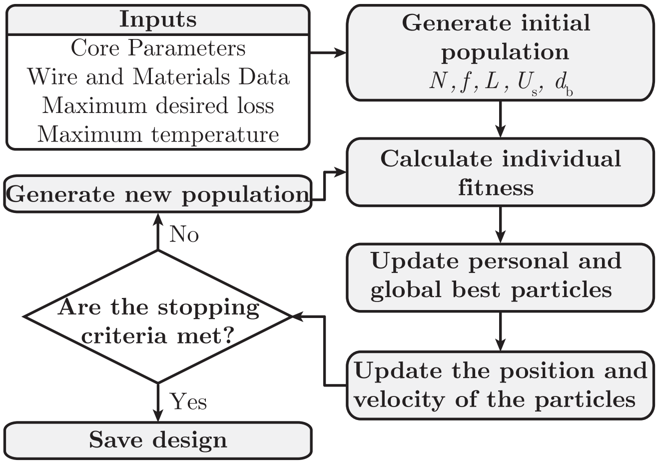

Fig. 2. Flowchart of the PSO algorithm used to minimize the ratio between copper and total losses.

TABLE I
EXAMPLES OF PARAMETER COMBINATIONS THAT RESULTS IN A 10-W CORE LOSS

N	f [kHz]	L [μH]	U_s [V]	d_b [mm]	P_c [W]	P_w [W]	P_t [W]	P_w/P_t [%]
5	750	6.66	89.61	1.45	10	0.256	10.26	2.50
14	750	52.20	250.91	1.45	10	0.091	10.09	0.90
25	750	166.46	448.05	1.45	10	0.051	10.05	0.51
25	143.65	166.46	300	1.45	10	0.273	10.27	2.66
14	750	52.20	89.61	1.00	10	0.132	10.13	1.30

Magnetics core. It is clear from the three first designs that a higher number of turns results in a smaller ratio P_w/P_t. However, a higher voltage is also necessary if the frequency is kept the same, which can make the voltage measurement more difficult and more susceptible to parasitic capacitances. Lower voltage can be used if the frequency is decreased, as in row four, but the ratio P_w/P_t becomes much higher. The last row shows how the wire diameter also influences the losses, and for the case in hand it should be maximized.

Necessary constraints such as maximum voltage can also be added to the optimization algorithm. For the case at hand, the number of turns was also constrained, resulting in a design with more space between the turns. This facilitates the attachment of the temperature sensor to the core. The second row represents the design obtained with the optimization for the core C0551952 A and dissipated power of 10 W. The constraints lead to a suboptimal design in terms of the ratio P_w/P_t but it is still acceptable.

A. *Impedance Matching*

Besides the poor power measurement accuracy resulting from the inductor low power factor, high excitation voltages are necessary for the core losses to reach the desired values, exceeding 400 V in some of the tested cases. Also, the influence of the probe's input capacitance on the phase of the measured waveforms could be noticed in several experiments, even with the use of differential probes. A capacitive impedance matching circuit, as shown in Fig. 1(b), minimizes the following problems:

1) The power factor at the measurement point is close to unity, greatly improving power measurement accuracy.
2) The voltage before the impedance matching circuit is much lower, facilitating the measurement.
3) The parasitic elements of the probe interfere less with the circuit, since the impedance is lower at the point of connection.
4) The maximum power of the amplifier can be transferred to the inductor, which is not possible when using only one capacitor in series.

There are different circuit configurations for impedance matching, some of them employing inductors. The most attractive for the case at hand is the one that employs only a series and a parallel capacitor, as shown in Fig. 1(b), since high-quality devices with very low losses are available. The DUT is represented by the series combination of its reactive X_L and resistive R_L impedance components. R_L represents all losses in the inductor. Once the inductor's model, as shown in Fig. 1(a), is obtained from the calculated losses and optimized operating point, the equivalent components can be calculated with

$$R_L = R_w + \frac{R_m \omega^2 L^2}{R_m^2 + (\omega L)^2}, \quad X_L = \frac{R_m^2 \omega L}{R_m^2 + (\omega L)^2}. \tag{1}$$

The capacitances C_s and C_p are calculated in order to make the real component of the equivalent impedance of the circuit equal to the output impedance of the source, and the imaginary component equal to zero, canceling the reactive power seen by the source. This results in

$$C_s = \frac{1}{\omega X_L - \omega\sqrt{R_L(Z_0 - R_L)}}, \quad C_p = \frac{\sqrt{R_L(Z_0 - R_L)}}{\omega R_L Z_0}. \tag{2}$$

Perfect impedance matching is only possible with this circuit when $R_L < Z_0$. Capacitors with low dissipation factor should be selected. Obtaining the desired capacitance values through capacitor associations in parallel is preferable, as ESL and ESR values are minimized. Given these characteristics, mica, porcelain, polypropylene, and air capacitors are the most suitable [23], [24]. Voltage stresses must also be taken into account when selecting the devices.

The current measurement must be made in the innermost part of the circuit, i.e., after the voltage measurement, especially if low-impedance voltage probes are used, which can drain significant amounts of current. Also, if a shunt resistor is used in the current measurement, it is necessary to subtract its voltage drop from the measured voltage.

B. *AC Measurement Probes*

Based on the previously discussed issues, the measurement probes must have a small input capacitance and wide bandwidth. The probes measurement derating as a function of the frequency is also an important specification since the amplitude of the high-frequency components can be quite high depending on the power imposed on the magnetic component core. In addition, voltage and current measurements must be well calibrated,

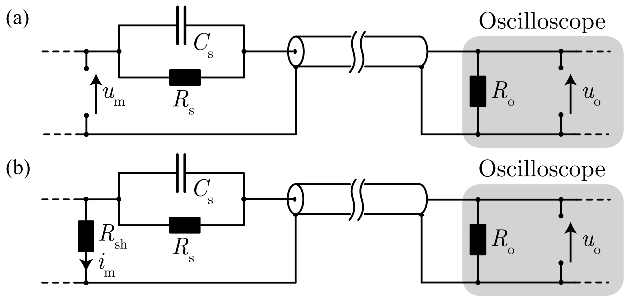

Fig. 3. (a) Low impedance voltage probe equivalent circuit. (b) Current probe equivalent circuit.

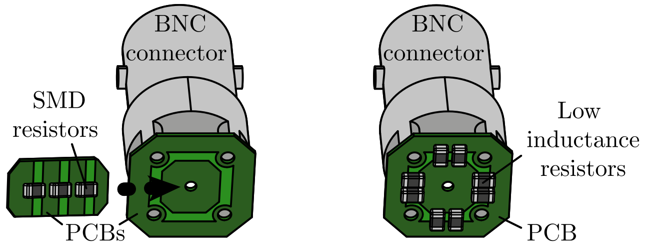

(a) (b)

Fig. 4. Proposed structure and assembly for (a) voltage probe and (b) current probe.

(a) (b)

Fig. 5. Probes used to measure. (a) Voltage. (b) Current.

since the displacement angle between these two quantities influences the processed active power, so measurement delays (intrinsic to the probes) can lead to significant uncertainties if not correctly compensated. As a result, commercially available probes capable of simultaneously meeting all requirements are costly.

As an alternative for voltage measurement, low-cost and low impedance custom passive probes can be built with very small input capacitance (less than 0.5 pF) and high bandwidth. The main disadvantage is that the circuit being tested must be able to drive a relatively low impedance without being heavily affected. If well designed, no compensation is required to match the oscilloscope impedance and unwanted effects such as high-frequency reflections that result in ringings, and spurious responses are avoided.

Shunt resistors are an attractive option for current measurements. They are typically cheaper than current probes and can have very high bandwidths. In addition, there is less susceptibility to external noise, and response delays are not directly a problem and depend only on the cable length. Thus, if the cable lengths of both probes are equal, no delay compensation is required. The main drawback is the equivalent series inductance (ESL), which can affect the measurement accuracy at high frequencies. Therefore, to minimize these problems, coaxial resistors are employed.

The low impedance voltage probe circuit is shown in Fig. 3(a). The resistor R_s is placed at the probe's input to form a resistive divider with the oscilloscope's $50\,\Omega$ input impedance. C_s is the parasitic capacitance of the resistor, and the cable is modeled as a transmission line. Similarly, the current measurement circuit is shown in Fig. 3(b). In this case, a $50\,\Omega$ resistor, R_s, is used to ensure a matched impedance on the shunt side. The capacitor C_s also represents the parasitic capacitance of the resistor.

Thus, the frequency response of the probes is

$$\frac{u_o(j\omega)}{u_m(j\omega)} = \begin{bmatrix} 1 & \frac{R_s}{j\omega C_s R_s + 1} \end{bmatrix} \cdot \mathbf{D} \cdot \begin{bmatrix} 1 \\ \frac{1}{R_o} \end{bmatrix} \tag{3}$$

$$\frac{u_o(j\omega)}{i_m(j\omega)} = \begin{bmatrix} \frac{1}{R_{sh}} & \frac{R_s}{R_{sh}(j\omega C_s R_s + 1)} \end{bmatrix} \cdot \mathbf{D} \cdot \begin{bmatrix} 1 \\ \frac{1}{R_o} \end{bmatrix} \tag{4}$$

with

$$\mathbf{D} = \begin{bmatrix} \cosh(\gamma l) & Z_0 \sinh(\gamma l) \\ \frac{\sinh(\gamma l)}{Z_0} & \cosh(\gamma l) \end{bmatrix}$$
$$\gamma = j\omega\sqrt{L_c C_c}. \tag{5}$$

where l represents the cable length and Z_0 is the characteristic impedance. L_c and C_c are the equivalent cable inductance and capacitance, respectively. The term $\sqrt{L_c C_c}$ corresponds to the cable propagation delay per unit length.

The voltage probe's physical structure was based on the design proposed in [25]. To minimize the contact resistance, the circuit is connected to an auxiliary printed circuit board (PCB) through two posts directly soldered in the circuit. The PCB is attached directly to the terminals of a BNC connector, where a coaxial cable is used to make the interface between the probe and the oscilloscope. An extra PCB is added to support the probe's resistors. Posts are soldered at both sides of the second board, connecting it with the circuit and the base PCB. Although the resistors are depicted in a serial connection, other configurations are possible. The assembly is depicted in Fig. 4(a).

If a commercial coaxial shunt is not available, the proposed structure can be used to assemble a shunt resistor, as shown in Fig. 4(b). In this case, low-inductance surface-mounted device (SMD) resistors must be connected in parallel and symmetrically arranged around the central terminal of the BNC connector aiming to reduce the equivalent ESL from the associations. Furthermore, the resistance value must be determined aiming for a tradeoff between power losses, sensitivity, and influence of the ESL for the frequencies and current levels typically applied in the experimental tests. The temperature coefficient is also an important criterion, which should be as low as possible.

The assembled voltage probe and the commercial coaxial shunt used can be seen in Fig. 5. The voltage probe was built from the series association of five equal 0612 SMD resistors.

TABLE II
MEASUREMENT CIRCUIT COMPONENTS SPECIFICATION

Voltage probe	
R_s	$5 \times 470\ \Omega \pm 0.5\%$, 1 W, ± 25 ppm (≈ 2.35 kΩ)
C_s	0.16 pF
Current probe	
R_sh	99.8 m$\Omega \pm 0.2\%$
R_s	$2 \times 100\ \Omega \pm 1\%$ ($\approx 50\ \Omega$)
C_s	0.4 pF
Cable and Oscilloscope	
R_o	50 Ω
C_c	202.10 pF
$\sqrt{L_\mathrm{c} C_\mathrm{c}}$	10.116 ns

Choosing the resistance is a tradeoff between too much attenuation and power dissipation. The chosen value was selected by limiting the expected power dissipation to a safe value.

Assuming that the parasitic capacitance of an SMD resistor size 1206 is around 0.2 pF [26] and four times greater for a resistor size 0612 (from the equivalence of the area and distance between the pads), an equivalent capacitance is estimated at $C_\mathrm{s} = 0.16$ pF. The current probe consists of a coaxial shunt resistor and two 1206 100 Ω resistors in parallel (to match the oscilloscope impedace), with an equivalent series capacitance estimated at approximately $C_\mathrm{s} = 0.4$ pF. More details about the components used are presented in Table II.

For both probe structures, R_o, C_c, and the propagation delay are exactly the same, since the same cable length and oscilloscope coupling are used. An RG58 C cable, with a characteristic impedance of $Z_0 = 50\ \Omega$ and two meters in length, was used. This results in an equivalent cable capacitance of $C_\mathrm{c} = 202.10$ pF and a total delay of 10.116 ns.

Based on the circuit of Fig. 1(b) and (3)–(5), the behavior of the probes can be analyzed. The probes' frequency responses are obtained and presented in Fig. 6. For each frequency point, the maximum and minimum values were obtained by optimizing all circuit elements within their tolerances for maximum absolute error. The attenuation values were normalized to facilitate comparison.

As shown in Fig. 6(a), the current probe attenuation has a flat response up to 100 MHz and, even in the worst cases, the uncertainty is less than 1%. The voltage probe also presents a flat response for the nominal values of the components up to 10 MHz, as seen in Fig. 6(a). The error is greater when compared to the current probe, reaching 7% in the worst-case scenario. This difference is explained by the almost perfect impedance matching of the current probe at both ends since R_o and R_s are equal to 50 Ω, while the voltage probe has an R_s almost 50 times greater and the gain flatness is heavily influenced by the parasitic capacitance C_s. On the other hand, the phase behavior is almost the same for both probes since the phase delay is caused mainly by the cable length. Therefore, as the power calculation depends on the angle of displacement between the voltage and current waveforms, the measurement delay does not affect the accuracy of the calculation. The phase difference between the two probes is shown in Fig. 7.

Up to 10 MHz, the displacement angle is still less than 2°, which has very little influence on the measurement accuracy when the power factor is close to unity [11]. If lower phase difference is desired at higher frequencies, it can be compensated by adjusting the C_s capacitance. To better understand this effect, the voltage probe circuit model can be simplified by modeling the cable as a simple capacitance, which results in the following transfer function:

$$\frac{u_\mathrm{o}(j\omega)}{u_\mathrm{m}(j\omega)} = \frac{R_\mathrm{o}}{R_\mathrm{o} + R_\mathrm{s}\dfrac{1 + j\omega C_\mathrm{c} R_\mathrm{o}}{1 + j\omega C_\mathrm{s} R_\mathrm{s}}}. \tag{6}$$

Note that for $C_\mathrm{s} R_\mathrm{s} = C_\mathrm{c} R_\mathrm{o}$ the transfer functions are reduced to a simple resistive divider, resulting in a flat response. Therefore, compensating the capacitance C_s may be necessary to ensure flatness, as exemplarily depicted in Fig. 8.

The curves show that too little capacitance results in poor bandwidth and phase delay, while too much capacitance amplifies high frequency and advances phase. Proper compensation allows for a good frequency response up to the GHz range [27].

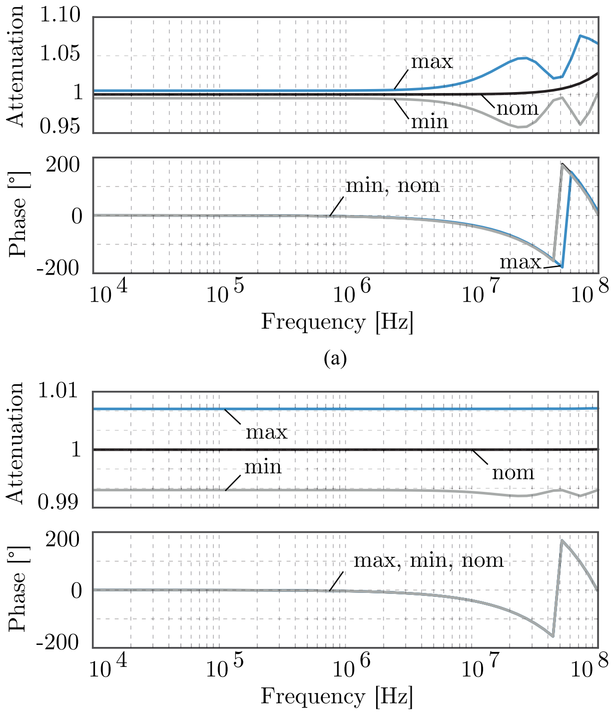

(a)

(b)

Fig. 6. Simulated frequency response of the proposed probes. (a) Voltage probe. (b) Current probe.

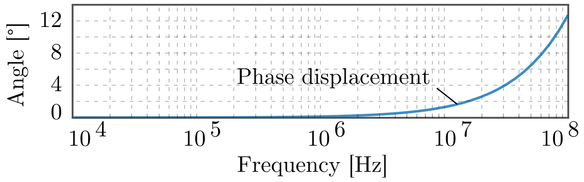

Fig. 7. Phase displacement between voltage and current measurements caused by the measurement delay.

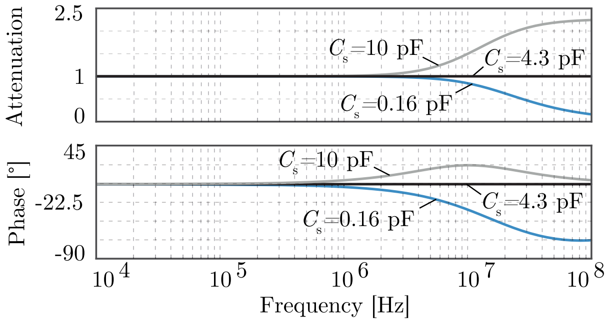

Fig. 8. Frequency response of the proposed voltage probe for a simplified model, considering different series capacitance values.

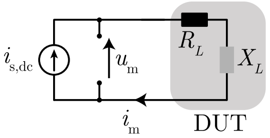

Fig. 9. Setup circuit of the individual test configuration to measure winding losses.

III. DC EXCITATION

The winding losses are imposed by controlling a dc current through the winding, as shown in Fig. 9. Maximizing the winding resistance ensures that moderate currents are enough to reach a power dissipation of a few tens of Watts. In addition, for a better assessment of the impact of winding losses on the magnetic component as a whole, it is preferable that the component has a high winding factor (corresponding to the amount of space in the core window that is occupied by the windings). The wire gauge was chosen considering a maximum number of turns, which was arbitrarily limited considering the maximum window factor, the minimum desired resistance, and also to facilitate the assembly process of the devices.

The challenges specifically related to the measurements of ac electric quantities are not present in this case. The main challenges in these tests are related to the quality of the power supply. Since the resistance of the winding is very small, the consequent voltage drop is also small, which can be difficult to measure if the signal is not clean. The noise generated by the power supply (e.g., switching noise) can also generate unwanted core losses. If necessary, a capacitor can be added in parallel to the power supply to minimize these problems.

A. DC Measurement Probes

For dc excitation experiments, it is typically necessary to ensure good accuracy in measuring voltages between a few tens of millivolts and a few volts, and currents ranging from a few amperes to tens of amperes depending on the DUT specification. This can be accomplished with common probes, as long as the excitation signal is properly filtered and good measurement practices are applied to the instrumentation process. In addition, the calibration of the probes is a simple process.

IV. TEMPERATURE MEASUREMENT

Measuring temperature in magnetic components can be a complex and difficult task, since intrusive techniques, such as drilling holes for placing sensors in the component's core may alter its performance. Moreover, some sensors (e.g., thermocouples) are more susceptible to interference.

A combination of RTDs and a thermographic camera was used to obtain the inductor's surface temperature distribution. Both RTDs and thermocouples have their readings' accuracy compromised by the thermal contact resistance related to their fixation on the DUT. However, RTDs proved to be a superior choice due to their smaller susceptibility to electromagnetic interference. To minimize the contact resistance issue, a thermal paste was used. Fixation is also an important factor in this regard. The use of tapes may impair the heat exchange between the component and the environment and may not ensure sufficient tightness between the RTD and the magnetic component. A less invasive alternative is the use of plastic cable ties, which can be relatively thin and interfere less with the heat transfer to the environment, in addition to providing contact pressure adjustment. The use of special glues, with high thermal conductivity and quick-drying, can also be an alternative as long as they are not placed between the sensor and the component and as long as the sensor is well pressed against the component. For the experimental tests, plastic cable ties altogether with thermal paste applied between the RTDs and the DUT were the method of choice, since during experimental testing it resulted in the best temperature accuracy and contact pressure.

Another important issue is that the temperature and heat flux distributions in the measured component may not be homogeneous, making it difficult to identify hot spots. Thus, to acquire precise temperature data, an IR thermographic camera was selected since it enables reliable and accurate nonintrusive surface temperature measurements, provided that the surface emissivity is known. To determine the surface emissivity of each component, a procedure recommended by the IR camera manufacturer [28] was adopted.

Altogether with the IR camera, RTD sensors were utilized to measure the following: ambient temperature inside the thermal chamber, blind spots of the thermal imaging, and surface temperature of the magnetic (for redundancy in the calculation of the surface's emissivity). All these temperature spots are important to portray an accurate thermal picture of the DUT.

V. EXPERIMENTAL SETUP

An automated apparatus was assembled for the experimental tests. The losses in the magnetic component are controlled and its temperature is measured after entering steady state. As previously discussed, the procedure was divided according to the main sources of losses in a magnetic component, being executed in two stages: only core losses (ac excitation) and only winding losses (dc excitation). Each experiment is executed several times until a repeatability criterion is met.

All equipment is controlled through LabVIEW, where a control loop was implemented. A PI controller compares the

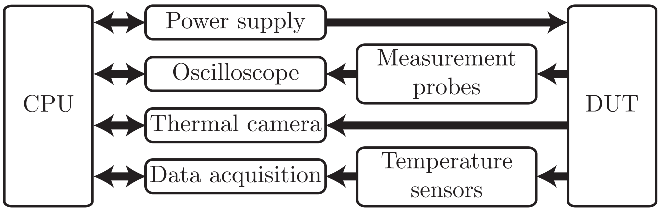

Fig. 10. Schematic diagram showing the data flow between the components of the experimental apparatus.

power measured by the oscilloscope against the reference and adjusts the amplifier gain, in case of ac excitation, or the dc current, in case of dc excitation, in order to ensure zero error. The tests are performed in descending order of power dissipation. If an estimation of the final temperature is available, either from a previous test or from a simulation, the test can be sped up by applying the maximum available power until the expected temperature is reached. From this instant on, the control loop is active and losses are controlled. When the derivative of the temperature is less than 0.03 °C/min and the largest temperature variation is less than 0.2 °C for both measurement methods (thermographic camera and RTD), the data recording starts. Then, during three minutes, the temperature data, the image from the thermographic camera, and the oscilloscope waveforms are stored. At the end of this step, the power is turned OFF, causing the component to cool down until the measured temperature is lower than the expected value for the next setpoint. The process is repeated until all points are tested.

The vertical scale of the oscilloscope is automatically adjusted so that all waveforms always occupy 90% of the screen, and thus a better accuracy as it is obtained. The management software has also been implemented with several protection layers, whereby the system is turned OFF if the temperature in the component exceeds a predefined value or an error code is identified, such as a communication failure with some equipment. To thermally insulate the DUT and avoid the influence of external disturbances, a thermal chamber of medium density fiberboard (MDF) material (15 mm thick) was built. All sides of the box interior were covered with a 10 mm thick thermally insulating, flameproof elastomeric foam with an emissivity close to unity.

The system structure is represented through the block diagram in Fig. 10. The control system is managed by the CPU. The control plant is relatively simple, so control structures without great complexity can be implemented.

Equipment descriptions and other supplemental information are listed below.

For the experimental tests with dc excitation:

1) Regatron TopCon Quadro (dc power supply)
2) LeCroy HRO 66Zi (12 Bits Oscilloscope)
3) LeCroy PP019 (Voltage probe)
4) LeCroy CP031 (Current probe)

For the tests with ac excitation:

1) Amplifier Research 75A250 (RF Amplifier)
2) Tektronix CFG253 (Function Generator)
3) LeCroy HRO 66Zi (12 Bits Oscilloscope)
4) Low input impedance designed probe (Voltage probe)
5) T&M Research SDN-414-10 (Coaxial shunt)

For temperature measurements:

1) FLIR SC655 (Thermographic Camera)
2) National Instruments SCXI-1000 Chassis and SCXI-1306 Terminal block (Data Acquisition)
3) SA1-RTD-4W-80 (RTD)

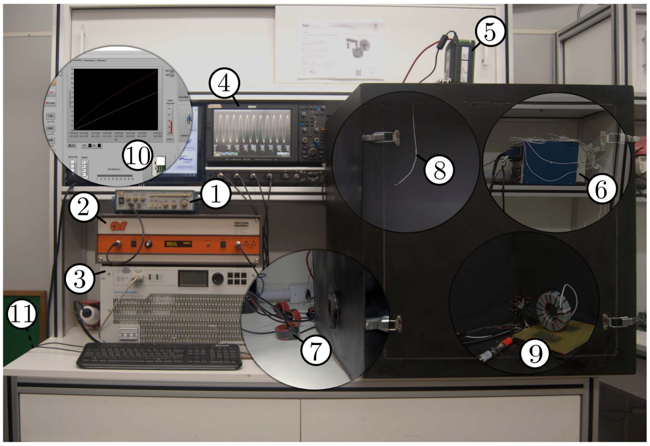

Fig. 11. Experimental bench setup for the temperature measurement test. (1) Function Generator. (2) RF Amplifier. (3) DC Power Supply. (4) Oscilloscope. (5) Thermal camera. (6) Data Acquisition System. (7) Common mode filters. (8) RTD for ambient air temperature. (9) DUT and measurement probes. (10) LabVIEW Software Interface. (11) CPU (under the table).

The assembled experimental bench is shown in Fig. 11. The image shows the core loss experiment in progress. In addition to the equipment used, it is also possible to see through the indications the software interface, the RTD position for measuring ambient temperature and the inductor instrumentation inside the thermal chamber. The image also highlights nanocrystalline cores that were added to the coaxial power and measurement cables, used to attenuate common mode components in tests with ac excitation.

A. *Power Measurement Uncertainty*

Given the differences between experiments with ac and dc excitation, such as the probes used, the power loss measurement uncertainty calculation needs to be performed independently for both cases. For each of them, the maximum uncertainty in power is obtained with the combination of parameters (measurement gains and component tolerances) that results in the highest deviation from the measured value.

From the analysis of Fig. 9, the relative uncertainty for the dc power measurement experiments can be calculated according to

$$\varepsilon_{\mathrm{p,dc}} = \max\left(\left|\frac{(U_{\mathrm{m}} \pm \varepsilon_{\mathrm{u}})(I_{\mathrm{m}} \pm \varepsilon_{\mathrm{i}})}{U_{\mathrm{m}} I_{\mathrm{m}}} - 1\right|\right) \qquad (7)$$

where U_{m} and I_{m} are, respectively, the values of the voltage and current in the DUT and, ε_{u} and ε_{i} are the voltage and current combined absolute maximum measurement uncertainty. They were calculated from the square root of the squared sum of the uncertainties from different sources [29]. Among these, there are systematic and random components. The former take into account the accuracy of the measurement probes, the oscilloscope gain, and dc offset uncertainty, the latter are related to the standard deviation of the measurements. The maximum relative uncertainty obtained for the dc losses measurement was 6.28%.

The ac power loss measurement uncertainty calculation needs to account for other effects. The frequency behavior of the system needs to be modeled and the tolerances of various components need to be considered. Thus, the uncertainty was calculated through an optimization routine with the objective of sweeping all possible combinations within the tolerances and uncertainties of all components and equipment to find the worst case. From the analysis of the circuits shown in Figs. 1(b) and 3, the following expression is obtained:

$$\varepsilon_{\mathrm{p,ac}} = \max\left(\left|\frac{\mathrm{Re}\{k_{\mathrm{v}}G_{\mathrm{v}}k_{\mathrm{i}}G_{\mathrm{i}}^{*}\}\mathrm{Re}\{U_{\mathrm{m}}I_{\mathrm{m}}^{*}\} - A - B}{\mathrm{Re}\{U_{\mathrm{m}}I_{\mathrm{m}}^{*}\} - R_{\mathrm{sh,nom}}|I_{\mathrm{m}}|^{2}} - 1\right|\right)$$

$$A = R_{\mathrm{sh}}|I_{\mathrm{m}}|^{2}$$

$$B = \mathrm{Im}\{k_{\mathrm{v}}G_{\mathrm{v}}k_{\mathrm{i}}G_{\mathrm{i}}^{*}\}\mathrm{Im}\{U_{\mathrm{m}}I_{\mathrm{m}}^{*}\} \quad (8)$$

where U_{m} and I_{m} are the RMS values of the voltage and current applied in the DUT; $R_{\mathrm{sh,nom}}$ is the shunt resistor's nominal value, while R_{sh} can assume any value among the shunt resistor resistance tolerance range. The voltage and current probe models, obtained in (3) and (4), are represented by G_{v} and G_{i}, respectively. In addition, k_{v} and k_{i} are factors that represent the oscilloscope measurement uncertainty. It is important to note that the oscilloscope's dc offset uncertainty should not be considered since ac coupling was used. The maximum relative uncertainty obtained for the ac losses measurement was 2.04% for the worst case tested.

VI. CFD MODELING

A. 3-D Models

The numerical model was implemented in the ANSYS Fluent 15.0 finite volume method (FVM) commercial software. Initially, 3-D models representing the C0551952 A Magnetics toroidal and the E55/28/21 Phillips core designed for the core and winding losses experiments were built in CAD software.

A special modeling strategy had to be adopted for the winding losses model. For the toroidal core, instead of modeling the winding as present in the DUT, a solid layer of copper with a volume equivalent to the winding used in experimental tests was generated and positioned above the bobbin to avoid meshing issues. On the other hand, for the E-core, the temperature rise data had proven to be quite sensitive to the winding modeling approach, so, in order to obtain the most accurate data, it was modeled as a group of wiring convoluted around the bobbin, with the same total volume as the winding used in the experimental tests.

A bottom plate composed of a 1.6 mm thick fiberglass plate was modeled as well. The air volume surrounding the component was modeled as an enclosure with the same internal dimensions of the insulated box. Fig. 12 shows the 3-D model of the inductor for the core and winding losses assessment.

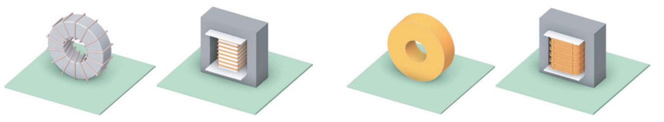

(a) (b)

Fig. 12. 3-D model of the toroidal and E-core inductors for CFD simulations with (a) core losses and (b) winding losses.

Symmetry conditions could be applied to reduce significantly the computational domain, and consequently, the computational cost. However, this was not carried out so that the temperature contour plots are comparable to the thermal imaging obtained through the infrared camera.

B. Meshing

The discretization of the domain was performed using a conformal poly-hexcore mesh, given that it reduces computational time and element count [30]. High-quality hexahedrons are utilized in the bulk regions of the domain and connected to isotropic polyprisms in the boundary layer through mosaic polyhedral elements. In addition, local sizing techniques and inflation elements were applied in regions with significant thermal gradients.

Mesh independence is paramount to guarantee the reliability of the numerical results and determine the ideal mesh setup to execute the CFD analysis. Stability and accuracy of the simulation can be severely affected by a low-quality mesh. Thus, a mesh convergence study was carried out based on two meshing parameters: 1) cell orthogonal quality and 2) skewness [31].

Three meshing levels were used for the convergence study: 1) a coarser; 2) a regular; and 3) a finer mesh. For the toroidal core, an optimal mesh with 2 196 587 cells was used for the core loss model, and a mesh with 298 386 cells was used for the winding loss model. As for the E-core, an optimal mesh with 10 482 217 cells was used for the core loss model and a 13 943 384 cells mesh was used for the winding loss model. The average orthogonal quality for all four meshes was very close to unity (minimum value was 0.87 for the toroidal core loss model) and average skewness close to zero (maximum value was 0.12 for the toroidal core loss model). The maximum difference between the different meshes was smaller than 0.2 °C.

The regular version of the meshes for all models was enough to ensure the accuracy at the temperatures acquired through the simulations. A higher number of elements was observed for the core model due to the necessity of meshing the few turns of the wiring around the core, once it has diminished dimensions and required very tiny cells to properly calculate heat transfer across it.

C. Setup

A steady-state, incompressible solver setup was implemented to provide the numerical solution of the losses in the toroidal and E-core inductors for the entire range of core and winding losses. Gravity acceleration and the energy equation model were activated. A pressure-based segregated solver was used with a

TABLE III
MATERIAL PROPERTIES CONSIDERED FOR THE SIMULATION (T_f IS THE FLUID TEMPERATURE IN K)

Material	Property		
Air	$\rho = (9 \cdot 10^{-6} {T_f}^2 - 9.4 \cdot 10^{-3} T_f + 3.1686)$ kg/m^3 $k = (7.5 \cdot 10^{-5} T_f + 3.69 \cdot 10^{-3})$ W/(m.K) $c_p = (4 \cdot 10^{-4} {T_f}^2 - 0.226 T_f + 1035.9)$ J/(kg.K) $\mu = (4.56 \cdot 10^{-8} T_f + 4.69 \cdot 10^{-6})$ kg/(m.s)		
Permalloy	ρ = 8200.0 kg/m^3	k = 8.0 W/(m.K)	c_p = 502.0 J/(kg.K)
Ferrite	ρ = 4850.0 kg/m^3	k = 3.9 W/(m.K)	c_p = 800.0 J/(kg.K)
Copper	ρ = 8978.0 kg/m^3	k = 387.6 W/(m.K)	c_p = 381.0 J/(kg.K)
Epoxy	ρ = 1150.0 kg/m^3	k = 0.17 W/(m.K)	c_p = 1100.0 J/(kg.K)
Fiberglass	ρ = 105.0 kg/m^3	k = 0.036 W/(m.K)	c_p = 795.0 J/(kg.K)
Polyethylene	ρ = 952.0 kg/m^3	k = 0.5 W/(m.K)	c_p = 1900.0 J/(kg.K)

TABLE IV
SUMMARY OF THE SIMULATION SETUP

Setup	Description
Domain	Solid (toroidal core, winding and fiberglass plate) and fluid (air)
Mesh	Poly-hexcore mesh grid
ρ, k, c_p, μ	Piece-wise linear functions of T_f for the fluid domain, constant for solid domains
Solver	Steady-state (pseudo-transient), incompressible, pressure-based solver, with gravity acceleration and energy equation activated
$P - \vec{v}$ coupling	Coupled
Turbulence model	4-equation, $\kappa - \omega$ SST with $\gamma - Re_\theta$ Transition model
Radiation model	Surface-to-surface radiation model
Boundary conditions	Volumetric heat generation at the core or winding prescribed temperature at the enclosure walls, and insulated at the bottom of the fiberglass plate
Discretization scheme	1st order upwind for initial (low Ra) iterations, 2nd order upwind for final convergence iterations
Relaxation factors	Momentum equations relaxed by a factor of 0.3, Energy equation relaxed by a factor of 0.9

coupled algorithm for pressure velocity coupling in a pseudo-transient approach. For the buoyancy formulation, a variable density approach was used with the air properties values for a temperature range of 250–450 K extracted from [32] and the properties of the inductor obtained from the specialized literature [32], [33], [34], [35]. A summary of the material properties used in the simulation is presented in Table III.

For the flow and heat transfer modeling, the $(\kappa - \omega)$ SST transition $(\gamma - Re_\theta)$ viscosity formulation was selected for all cases, once it was successful at producing accurate and coherent results for natural convection in the laminar-turbulent transition region $(Ra \approx 10^7)$ [36], [37]. The surface-to-surface radiation model was selected; in this model, view factors are calculated based on the relative positions of the surfaces and their emissivities.

The boundary conditions were as follows:

1) a uniform volumetric heat generation for the core losses and another for the winding losses;
2) fixed temperatures at the enclosure walls corresponding to the ambient temperature measured experimentally;
3) inlet velocity at the side walls of the enclosure with a y-velocity component of 0.05 m/s and a gauge pressure of 0 Pascals at the top wall (to help promote natural convection inside the enclosure).

The bottom surface of the fiberglass plate is assumed thermally insulated (no heat flux). Power losses of 2, 4, 6, 8, and 10 W were considered for the core and winding losses. The following emissivity values (calculated experimentally with the IR camera) were set: 1 for the walls of the enclosure; 1 for the surface of the toroidal inductor and the copper; 0.95 for the fiberglass; 0.925 for the ferrite; 0.91 for the spool. A summary of the model setup is presented in Table IV .

D. Solution Scheme

A special solution procedure was adopted, consisting of a low Rayleigh number scheme during the first 50 iterations with a reduced acceleration of gravity ($g = -0.00981$ m/s^2). During this initial part, a first-order upwind interpolation scheme is applied to all conservation equations. In the following 50 iterations, a high Rayleigh number scheme is implemented by setting $g = -9.81$ m/s^2 and first-order upwind interpolation scheme in all conservation equations. Finally, for the remaining 40 iterations, another high Rayleigh number setup with second-order upwind schemes is used in the conservation equations.

Due to the highly nonlinear energy and momentum coupling present in boundary-induced flow situations, under-relaxation factors were applied in the Navier–Stokes and energy equations to obtain stability and convergence (0.3 and 0.9, respectively). To check for convergence, the maximal surface temperature and volume-averaged temperature in the core and windings were monitored, together with the conservation equations residuals, which had to be lower than 10^{-3} for the momentum balance equations and 10^{-6} for the energy and turbulence modeling equations. Pseudotransient simulations for conjugate heat transfer generally require few iterations to converge; however, they demand an elevated computational cost. Thus, a computational cluster with 72 processing cores and 512 GB of RAM memory was used to carry out the simulations.

VII. RESULTS AND DISCUSSION

For the experimental validation tests, toroidal and E-core inductors were designed according to the procedure previously described for the C0551952 A Magnetics and the E55/28/21 Phillips cores, respectively. The optimization procedure applied to the core loss test resulted in a toroidal inductor with 14 turns and wire gauge (AWG) 15, with an ac excitation of 750 kHz. On the other hand, the optimization resulted in 9 turns, wire gauge (AWG) 15, and an ac excitation of 120 kHz for the E-core inductor. For the winding loss test, a toroidal inductor with 156 turns and AWG 17 and an E-core inductor with 137 turns and AWG 17 were assembled.

The setup for all experiments can be seen in Fig. 13.

The maximum surface temperature rise obtained numerically and experimentally, for the core and winding losses, are presented in Fig. 14. The relative uncertainties calculated for the temperature and power measurements in the experiments are also highlighted in the figures. The shaded area indicates the

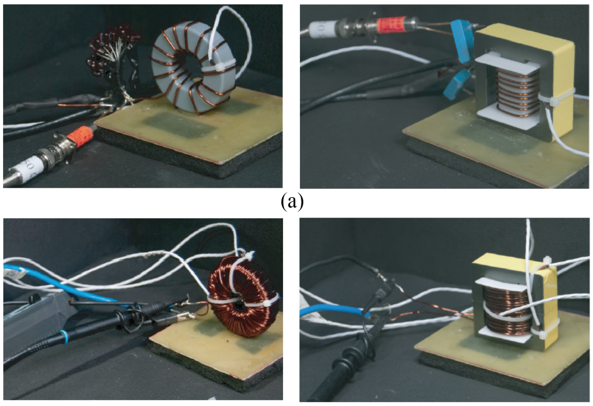
(a)

(b)

Fig. 13. Setup of the experimental tests for toroidal and E-core inductors for (a) core losses and (b) winding losses.

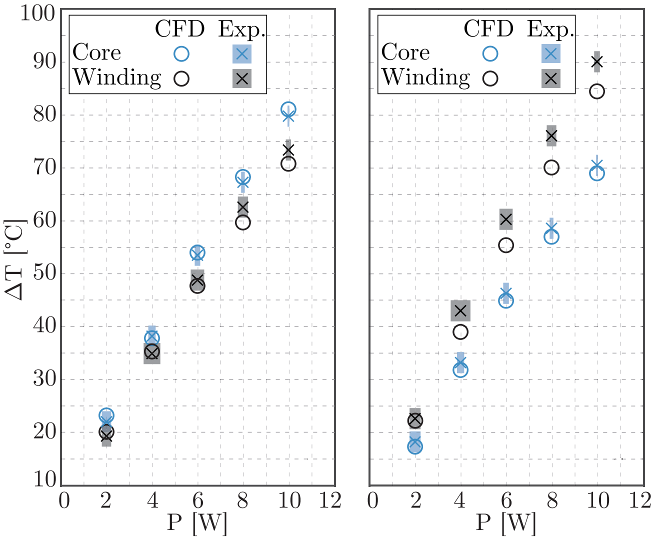

(a) (b)

Fig. 14. Maximum surface temperature rise for the winding and core losses obtained numerically and experimentally for (a) toroidal inductor and (b) E-core inductor.

region of measurement uncertainty (with reference to the center of the markers).

An encouraging agreement is observed for both loss types in the toroidal core case, as seen in Fig. 14(a). The highest deviation observed was 5% in the temperature rise, or a 2.9 °C absolute error, for the winding losses. This deviation is probably due to the approximation of the winding modeling to simplify the simulations and a not perfectly homogeneous thermal distribution, that was not considered in the simulations. However, they are close to the IR camera experimental uncertainty of 2 °C.

On the other hand, the temperature data for the core loss on the E-core inductor are excellent, with a maximum deviation of 1.7 °C, as shown in Fig. 14(b). Nonetheless, a steeper error was found for the winding loss, with a maximum deviation of 6.0 °C between experimental and numeric data, or 7.9%. This can be explained by a combination of several factors. The uncertainty on the temperature and power measurements directly impacts the inductor temperature rise, which is higher in the dc excitation tests as shown previously. However, the biggest difference can be linked to the heterogeneous temperature distribution, which is considerably worse when compared to the toroidal inductor. Still, for tests with dc excitation, the plastic bobbin becomes an additional problem due to the existence of air gaps between this component and the core of the DUT, which increases the thermal resistance and decreases the heat dissipation in the core, leading to a higher temperature rise in the winding. These small gaps are difficult to model perfectly in CFD simulations.

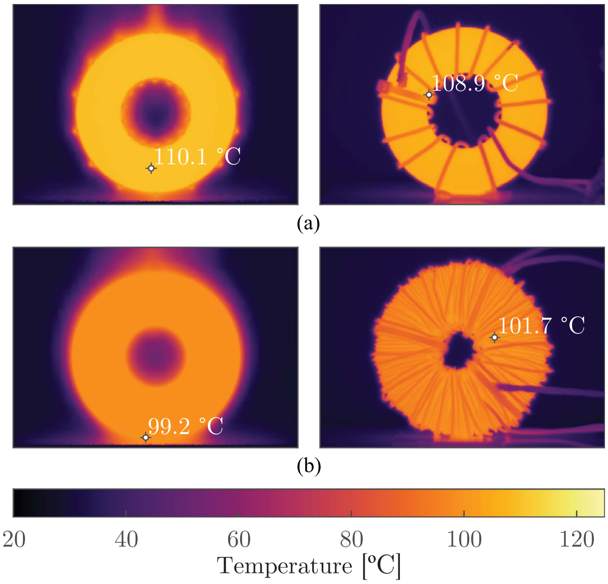

(a)

(b)

Fig. 15. Temperature distribution in the toroidal inductor with a 10 W power loss obtained through CFD simulation (leftmost figures) and camera thermal imaging (rightmost figures) for: (a) AC excitation and (b) DC excitation.

In order to gain further insight into the temperature rise of the toroidal and E-core inductors, for power losses at the core and winding, temperature distribution obtained through thermal infrared imaging and CFD simulation are presented, considering a 10-W power loss and an ambient temperature of 28 °C, in Figs. 15 and 16.

The temperature distribution obtained through thermal imaging shows a strong resemblance with the contour plots provided by the numerical simulations. The difference in the temperature field around the inductor, when comparing both images, exists because the simulation is able to obtain the temperature distribution of the airflow, which doest not happen with thermal imaging. Minor temperature deviations between them are present due to the fact that the power losses at the toroidal and E-core inductor are not perfectly homogeneous, unlike the simulations, which rely on a homogeneous volumetric loss. This effect is more pronounced for the E-core inductor, as can be seen in the figures.

Finally, the comparison between the two temperature distribution graphs with Fig. 14 reinforces the consistency of the presented results. Despite the larger deviations for the dc excitation tests on the E-core inductor, the errors are less than 10% and could be explained by several factors. Furthermore, an excellent agreement is observed between simulation and experiment for all other cases, thus validating the proposed methodology.

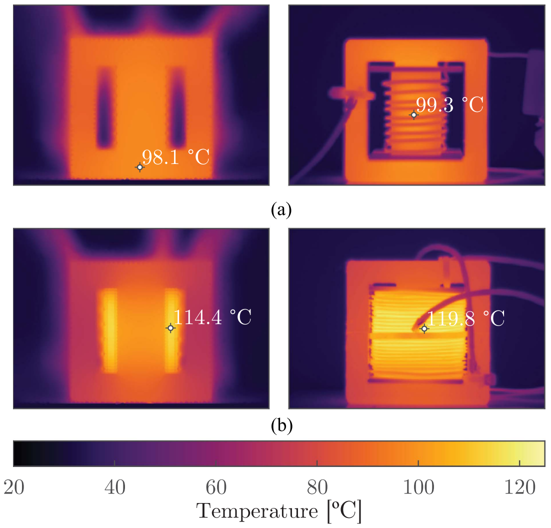

Fig. 16. Temperature distribution in the E-core inductor with a 10 W power loss obtained through CFD simulation (leftmost figures) and camera thermal imaging (rightmost figures) for (a) AC excitation and (b) DC excitation.

VIII. CONCLUSION

A procedure for the thermal characterization of magnetic components with distinct inputs for core and winding losses was proposed and validated. A constant power is imposed on the core and on the winding, one at a time, and the temperature rise is measured for both cases. The obtained results can also be used to validate thermal models (analytical or CFD) by comparing experimental and calculated values.

Imposing winding losses can be easily accomplished by injecting a dc current that results in the desired total loss in a closed-loop manner. Uncertainty analysis shows that a relatively small power measurement error (6.28% for the presented setup) can be obtained with common current and voltage probes. Most of the error is caused by the uncertainty in the offset (vertical position) error of the oscilloscope.

Core losses, on the other hand, are more difficult to measure and impose. It is proposed that the design of the winding should be optimized in the sense of minimum loss so that most of the temperature rise comes from the core. This also helps with the measurement of the core losses, since there is no need to use an auxiliary winding to measure the flux variation in the core, as commonly done. Using only one winding reduces the errors associated with the capacitive coupling between the two windings. This work also proposes the use of an impedance-matching network between the RF amplifier and the inductor under test. The first advantage is a much smaller power measurement error since the power factor is raised to unity, theoretically. The second advantage is the capability of transferring full power from the amplifier to the magnetic component, which can not be achieved with only one series capacitor. The use of low-impedance low-cost voltage probes with low input capacitance, predictable frequency response and delay is proposed. A detailed error analysis of the power measurement system composed of the designed voltage probe and a shunt-based current probe resulted in an uncertainty of 2.04%.

Acquiring temperature through an infrared camera proved to be a more promising alternative for magnetic components when compared to other experimental setups due to the deviation in temperature caused by thermal contact resistance when using direct measuring devices such as thermocouples or RTDs. Also, electromagnetic interference is usually an issue with these devices due to the high-frequency strong electric and magnetic fields present close to the device.

Finally, a good agreement between results obtained through thermal imaging and the temperature contour plots acquired from the simulations. The slight differences observed in the temperature distribution patterns can be attributed to the not perfectly homogenous loss distribution in the DUT, not observed in the CFD model, since a homogeneous power loss was considered. Furthermore, the experimental uncertainty of the power losses, shown in Fig. 14, might have also influenced this deviation in temperature data.

REFERENCES

[1] C. Xiao, G. Chen, and W. G. H. Odendaal, “Overview of power loss measurement techniques in power electronics systems,” *IEEE Trans. Ind. Appl.*, vol. 43, no. 3, pp. 657–664, May/Jun. 2007.

[2] R. Linkous, A. W. Kelley, and K. C. Armstrong, “An improved calorimeter for measuring the core loss of magnetic materials,” in *Proc. 15th Annu. IEEE Appl. Power Electron. Conf. Expo.*, 2000, vol. 2, pp. 633–639.

[3] J. K. Bowman, R. F. Cascio, M. P. Sayani, and T. G. Wilson, “A calorimetric method for measurement of total loss in a power transformer,” in *Proc. Rec. 22nd Annu. IEEE Power Electron. Specialists Conf.*, 1991, pp. 633–640.

[4] D. Rothmund, D. Bortis, and J. W. Kolar, “Accurate transient calorimetric measurement of soft-switching losses of 10-kV SiC mosfets and diodes,” *IEEE Trans. Power Electron.*, vol. 33, no. 6, pp. 5240–5250, Jun. 2018.

[5] P. Papamanolis, T. Guillod, F. Krismer, and J. W. Kolar, “Transient calorimetric measurement of ferrite core losses up to 50 MHz,” *IEEE Trans. Power Electron.*, vol. 36, no. 3, pp. 2548–2563, Mar. 2021.

[6] J. Mühlethaler, J. Biela, J. W. Kolar, and A. Ecklebe, “Improved core loss calculation for magnetic components employed in power electronic system,” in *Proc. 26th Annu. IEEE Appl. Power Electron. Conf. Expo.*, 2011, pp. 1729–1736.

[7] K. Venkatachalam, C. R. Sullivan, T. Abdallah, and H. Tacca, “Accurate prediction of ferrite core loss with nonsinusoidal waveforms using only steinmetz parameters,” in *Proc. IEEE Workshop Comput. Power Electron.*, 2002, pp. 36–41.

[8] T. Shimizu and K. Ishii, “An iron loss calculating method for AC filter inductors used on PWM inverters,” in *Proc. 37th IEEE Power Electron. Specialists Conf.*, 2006, pp. 1–7.

[9] W. Shen, F. Wang, D. Boroyevich, and C. W. Tipton, “Loss characterization and calculation of nanocrystalline cores for high-frequency magnetics applications,” in *Proc. 22nd Annu. IEEE Appl. Power Electron. Conf. Expo.*, 2007, pp. 90–96.

[10] A. Brockmeyer, “Experimental evaluation of the influence of DC-premagnetization on the properties of power electronic ferrites,” in *Proc. Appl. Power Electron. Conf.*, 1996, vol. 1, pp. 454–460.

[11] V. J. Thottuvelil, T. G. Wilson, and H. A. Owen, “High-frequency measurement techniques for magnetic cores,” *IEEE Trans. Power Electron.*, vol. 5, no. 1, pp. 41–53, Jan. 1990.

[12] M. Mu, Q. Li, D. J. Gilham, F. C. Lee, and K. D. T. Ngo, “New core loss measurement method for high-frequency magnetic materials,” *IEEE Trans. Power Electron.*, vol. 29, no. 8, pp. 4374–4381, Aug. 2014.

[13] M. Milutinov, N. Blaz, and L. Zivanov, “Ferrite core loss measurement issues and technique,” in *Proc. 18th Int. Symp. Power Electron. - Ee*, 2015, pp. 1–5.

[14] F. Dong Tan, J. L. Vollin, and S. M. Cuk, “A practical approach for magnetic core-loss characterization,” *IEEE Trans. Power Electron.*, vol. 10, no. 2, pp. 124–130, Mar. 1995.

[15] Y. Han, G. Cheung, A. Li, C. R. Sullivan, and D. J. Perreault, “Evaluation of magnetic materials for very high frequency power applications,” in *Proc. IEEE Power Electron. Specialists Conf.*, 2008, pp. 4270–4276.

[16] *Integrated Circuits Thermal Test Method Environmental Conditions—Natural Convection (Still Air)*, Standard 51-2A:2008, JEDEC Solid State Technology Association, Arlington, VA, USA, Jan. 2008.
[17] V. H. Adams, D. L. Blackburn, Y. K. Joshi, and D. W. Berning, "Issues in validating package compact thermal models for natural convection cooled electronic systems," *IEEE Trans. Compon., Packag., Manuf. Technol.: Part A*, vol. 20, no. 4, pp. 420–431, Dec. 1997.
[18] M. Touré, P. Souaré, and J. Sylvestre, "Best practices for thermal modeling in microelectronics with natural convection cooling: Sensitivity analysis," *J. Electron. Cooling Thermal Control*, vol. 10, pp. 15–33, Jun. 2021.
[19] A. Bairi, "Thermal design of tilted electronic assembly with active QFN16 package subjected to natural convection," *Int. Commun. Heat Mass Transfer*, vol. 66, pp. 240–245, Aug. 2015.
[20] C. P. Steinmetz, "On the law of hysteresis," *Trans. Amer. Inst. Elect. Engineers*, vol. IX, no. 1, pp. 1–64, 1892.
[21] J. A. Ferreira, "Improved analytical modeling of conductive losses in magnetic components," *IEEE Trans. Power Electron.*, vol. 9, no. 1, pp. 127–131, Jan. 1994.
[22] J. Kennedy and R. Eberhart, "Particle swarm optimization," in *Proc. Int. Conf. Neural Netw.*, 1995, vol. 4, pp. 1942–1948.
[23] *R. S. C. Test*, "Power magnetics design and measurement of power magnetics," 2011. [Online]. Available: http://thayer.dartmouth.edu/inductor/design_and_meas.pdf
[24] G. L. Johnson, "Solid state tesla coil," 2001, pp. 1–152. [Online]. Available: http://www.g3ynh.info/zdocs/refs/Tesla/Johnson2001_ssTeslacoil.pdf
[25] D. Smith, *High Frequency Measurements and Noise in Electronic Circuits*. New York, NY, USA: Springer, 1992.
[26] U. Tietze, C. Schenk, and E. Gamm, *Electronic Circuits: Handbook for Design and Application*. 2nd ed. Berlin, Germany: Springer, 2015.
[27] "Probing tutorial," Lecroy, Tech. Rep., *Application Note 016*. [Online]. Available: http://cdn.teledynelecroy.com/files/appnotes/lecroy_probing_tutorial_appnote016.pdf
[28] *User's Manual FLIR ETS3xx Series*, FLIR, Manual. [Online]. Available: https://flir.netx.net/file/asset/11358/original/attachment
[29] *Evaluation of Measurement Data — Guide to the Expression of Uncertainty in Measurement*, Standard JCGM100:2008, Bureau International des Poids et Mesures, Sèvres, France, 2008.
[30] K. Zore, B. Sasanapuri, G. Parkhi, and A. Varghese, "ANSYS mosaic poly-hexcore mesh for high-lift aircraft configuration," in *Proc. 21st Annu. CFD Symp.*, 2019, pp. 1–11.
[31] O. Zikanov, *Essential Computational Fluid Dynamics*. 1st ed. Hoboken, NJ, USA: Wiley, 2010.
[32] F. P. Incropera, D. P. DeWitt, T. L. Bergman, and A. S. Lavine, *Fundamentals of Heat and Mass Transfer*. 6th ed. Hoboken, NJ, USA: Wiley, 2006.
[33] M. S. Rylko, "Magnetic materials and soft-switched topologies for high-current DC-DC converters," *Ph.D. dissertation*, Dept. Elect. Electron. Eng., Univ. College Cork, Cork, Ireland, 2011.
[34] Y. Itoh, S. Kimura, J. Imaoka, and M. Yamamoto, "Inductor loss analysis of various materials in interleaved boost converters," in *Proc. IEEE Energy Convers. Congr. Expo.*, 2014, pp. 980–987.
[35] *E. METALS*, "Permalloy 80," 1999. [Online]. Available: https://www.espimetals.com/index.php/technical-data/175-permalloy-80
[36] Z. Zhai, Z. Zhang, W. Zhang, and Q. Y. Chen, "Evaluation of various turbulence models in predicting airflow and turbulence in enclosed environments by CFD: Part 1–Summary of prevalent turbulence models," *HVAC&R Res.*, vol. 13, no. 6, pp. 853–870, Nov. 2007.
[37] M. Abdollahzadeh, M. Esmaeilpour, R. Vizinho, A. Younesi, and J. C. Pàscoa, "Assessment of RANS turbulence models for numerical study of laminar-turbulent transition in convection heat transfer," *Int. J. Heat Mass Transfer*, vol. 115, no. Part B, pp. 1288–1308, Dec. 2017.

Bruno Bertoldi (Graduate Student Member, IEEE) received the B.Sc. degree from the State University of Santa Catarina (UDESC), Joinville, Brazil, in 2017, and the M.Sc. degree from the Federal University of Santa Catarina, Florianopolis, Brazil, in 2021, both in electrical engineering.

He is currently working on projects with the Federal University of Santa Catarina and is a Consultant for power electronics companies. His research interests include EMI, optimization processes, and filter design for power converters.

Lucas Andrade Militão (Graduate Student Member, IEEE) received the B.S. degree in mechanical engineering from the Federal Center of Technological Education of Minas Gerais and California State University, Chico, CA, USA, in 2014, and the M.S. degree in mechanical engineering, in 2019, from the Federal University of Santa Catarina (UFSC), Florianopolis, Brazil where he is currently working toward the Ph.D degree in mechanical engineering.

His research interests include electronics cooling, electrothermal network modeling, and computational fluid dynamics.

Gean Jacques Maia de Sousa (Member, IEEE) received the bachelor's degree in electrical engineering from the Federal University of Ceará, Brazil, in 2010, and the master's and doctoral degrees in electrical engineering from the Federal University of Santa Catarina, Florianopolis, Brazil, in 2014 and 2022, respectively.

He is currently a Postdoctoral Researcher with the Chair of High-Power Converters, Technical University of Munich, Munich, Germany. His main research interests include multilevel converters and modeling and control for power electronics.

Jader Riso Barbosa Jr. received the Ph.D. degree in mechanical engineering from Imperial College London, London, U.K.

He is currently a Professor with the Department of Mechanical Engineering, Federal University of Santa Catarina (UFSC), Florianopolis, Brazil. He has authored or coauthored more than 300 scientific papers in indexed journals and international peer-reviewed conferences and has advised/coadvised 52 theses/dissertations. His research interests include fluids engineering and emerging cooling technologies.

Dr. Barbosa Jr. is a Member of the Scientific Council of the International Center for Heat and Mass Transfer (ICHMT) and the President of the Assembly of World Conferences on Experimental Heat Transfer, Fluid Mechanics and Thermodynamics. He is the Director of the National Institute of Science Technology in Cooling and Thermophysics (INCT-RT), UFSC. He is Co-Editor-in-Chief for the *Journal of the Brazilian Society of Mechanical Sciences and Engineering* (Springer Nature) and Subject Editor for *Applied Thermal Engineering* (Elsevier).

Marcelo Lobo Heldwein (Senior Member, IEEE) received the B.S. and M.S. degrees in electrical engineering from the Federal University of Santa Catarina (UFSC), Florianopolis, Brazil, in 1997 and 1999, respectively, and the Ph.D. degree in electrical engineering from the Swiss Federal Institute of Technology (ETH Zürich), Zürich, Switzerland, in 2007.

From 1999 to 2003, he was with industry, including research and development activities at the Power Electronics Institute, Brazil and Emerson Network Power, Brazil and Sweden. From 2007 to 2009, he was a Postdoctoral Fellow with the ETH Zürich and the UFSC. From 2010 to 2022, he was a Professor with the Department of Electronics and Electrical Engineering, UFSC. He is currently the Head of the Chair of High-Power Converter Systems (HLU), Technical University of Munich (TUM), Munich, Germany. His research interests include power electronics, advanced power distribution technologies, and electromagnetic compatibility.

Dr. Heldwein is a Member of the Brazilian Power Electronic Society (SOBRAEP), and a Member of the Advisory Board of PCIM Europe.